Friction https://mc03.manuscriptcentral.com/friction
https://doi.org/10.26599/FRICT.2026.9441279

Research Article

A fractal contact-transfer film framework for wear evolution and lifetime assessment of composite piston rings in Stirling Engines

Dongya Yang[1*], You Kang[1,2], Gengrui Zhao[2*], Honggang Wang[2*], Huan Gong[3], Huiya Yang[3], Wenguang Liu[2], Gui Gao[2], Junfang Ren[2], Xiao Li[1]

[1] School of Mechanical and Electronical Engineering, Lanzhou University of Technology, Lanzhou 730050, China

[2] Key Laboratory of Science and Technology on Wear and Protection of Materials, Lanzhou Institute of Chemical Physics, Chinese Academy of Sciences, Lanzhou 730000, China

[3] Shanghai Marine Diesel Engine Research Institute, Shanghai 200000, China

Corresponding author: Dongya YANG: yangdy@lut.edu.cn

Gengrui ZHAO: zhaogengrui@licp.cas.cn

Honggang WANG: hgwang@licp.cas.cn

Received: January 5, 2026; Revised: May 9, 2026; Accepted: June 9, 2026

Abstract: Understanding and predicting wear evolution in composite piston rings for Stirling engines is challenging due to multiscale rough surface contact and dynamic transfer film formation. This study develops a unified wear prediction framework integrating fractal contact theory with visualized transfer film characterization. Fractal parameters (D, G) capture initial asperity-dominated contact, while a transfer film index (TFI) is synthesized from coverage, connectivity, and porosity with weights ω_C = 0.573, ω_k = 0.334, ω_H = 0.093 to quantify film structure and load-bearing capacity. Experimental results show the transfer film evolves from discrete to dense-continuous, with TFI increasing from 0.0427 to 0.8083. TFI correlates negatively with the friction coefficient ($R^2 \approx 0.91$) and governs wear rate attenuation, where TFI ≥ 0.7 indicates a stable low-wear regime. Incorporating TFI improves wear rate prediction accuracy from R^2 = 0.9149 to 0.9545 (relative error: 4.85~31.48%), which captures the full wear evolution. The framework elucidates the transition from asperity contact to transfer film-dominated lubrication, and its forward-validation against extended-time experimental data demonstrates its potential for reliable lifetime assessment of composite piston rings in Stirling engines.

Keywords: Stirling engines; Dynamic transfer film; Fractal parameters; Transfer film index; Wear prediction

1. Introduction

The piston ring seal is the core contact-type sealing structure of Stirling engines, playing a decisive role in engine efficiency and operational reliability. It is primarily installed at the critical interface between the piston and cylinder wall [1][2]. Stirling engines are widely used in specialized fields such as distributed energy supply systems and deep-space exploration equipment, operating under harsh service conditions: intense high-low temperature cycling, frequent operating state transitions, and corrosive working gas environments. These severe conditions impose stringent requirements on the sealing stability, structural fatigue resistance, and wear durability of piston rings [3][4]. During engine operation, the piston's reciprocating motion drives the piston ring to move synchronously. Meanwhile, the gas pressure in the working chamber further enhances the conformity between the piston ring and cylinder wall. This forms a composite sealing mechanism dominated by contact sealing and supplemented by micro-gap gas film sealing. However, long-term service exposes the piston ring to irregular wear and progressive failure, caused by high-frequency reciprocating motion and microscopic surface topography deviations of the cylinder wall. Such wear impairs the sealing interface's connectivity and leads to gas leakage, which not only reduces engine output power and energy utilization efficiency but also accelerates lubricant degradation due to gas blow-by into the crankcase. In severe cases, this can trigger critical failures such as piston seizure and cylinder scuffing. Therefore, systematic research on the wear characteristics of piston ring seals in Stirling engines is of significant engineering value for improving operational reliability and extending service life.

To enhance the service life of piston rings under harsh operating conditions, the ring materials must exhibit adequate thermal stability and a low wear rate [5][6][7]. For sealing ring material selection, studies by MTI Corporation (USA) have confirmed that polytetrafluoroethylene (PTFE)-filled composites inherently possess low friction coefficients and reduced wear rates. Thanks to their excellent tribological performance, wear resistance, and chemical stability, PTFE-based composites have been widely adopted in engineering scenarios requiring high wear resistance, such as seals, bearings, gears, and valves [8]. As a self-lubricating material, PTFE performs exceptionally well under dry sliding conditions [9], leading to its extensive application in aerospace, automotive, electronics, and medical device industries [10][11]. Numerous studies have shown that adding solid fillers to the PTFE matrix can effectively enhance its tribological properties. Yang *et al*. [12] for instance, investigated the frictional behavior of PTFE-based composite sealing components and identified their wear mechanisms through experimental analysis, finding that modified PTFE-based composites exhibited significantly improved tribological performance, resulting in enhanced wear resistance and extended service life. However, despite the outstanding performance of PTFE-based composites in various applications, their long-term wear behavior remains highly uncertain under the complex cyclic conditions of Stirling engines. Relying solely on material modification and friction-wear experiments is insufficient to predict this long-term wear behavior accurately. In actual operation, the piston ring-cylinder liner interface exhibits distinct multiscale rough surface contact characteristics, and the microscopic contact state, load distribution, and material deformation continuously evolve with operating conditions and service time. Experimental methods are not only costly and time-consuming but also limited in quantitatively evaluating wear performance under varying operating conditions. Establishing a wear rate prediction model with a clear physical basis is therefore crucial for optimizing the design and assessing the service life of piston ring sealing structures.

Against this background, research focus has gradually shifted from tribological performance characterization to theoretical modeling of wear rates. For PTFE-based composites in particular, wear behavior is governed not only by asperity contact and deformation mechanisms but also by the characteristics of transfer films formed during sliding. These dual governing factors make the wear mechanism of PTFE-based composites more complex. As a result, higher demands are posed on the applicability of conventional wear models. Current research has predominantly centered on analyzing surface tribological performance, with relatively limited studies addressing volumetric wear rate prediction. Existing wear prediction models include the fractal contact model for rough surfaces originally proposed by Majumdar and Bhushan (the MB model) [13]. Building on this framework, Yan *et al.* [14] developed a three-dimensional fractal contact model based on an improved Weierstrass-Mandelbrot (W-M) function. These models primarily account for the elastic and fully plastic deformation regimes of asperities during sliding contact, yet the elastoplastic deformation regime, where a considerable portion of asperities actually reside lacks explicit consideration, inherently constraining their predictive accuracy. Zhou *et al*. [15] were the first to integrate fractal contact theory with Archard's wear law, proposing a fractal-based wear model for mechanical contact surfaces. Ding *et al.* [16] later established quantitative relationships between wear rate and fractal parameters. However, these models all rely on the MB contact framework, and due to the limitations of traditional contact mechanics, they cannot fully describe the complete transition of asperities from elastic to fully plastic deformation. With further advancements in contact modeling, Etsion *et al.* [17][18] employed an improved W-M function to account for all deformation regimes of asperities during sliding, including elastic, elastoplastic, and fully plastic deformation. This comprehensive consideration led to a substantial improvement in prediction accuracy compared with earlier models. Nevertheless, subsequent models derived from Archard's law and the Greenwood-Williamson (GW) framework primarily focus on the prediction of wear depth and do not adequately incorporate the influence of transfer film formation.

Transfer films, which develop during the sliding process, play a critical role in lubrication and surface protection and thus exert a significant influence on wear behavior [19][20]. Recent studies have made important progress in the quantitative characterization and mechanistic interpretation of transfer films. Haidar *et al.* [21] systematically evaluated multiple transfer-film quality metrics, including thickness, area fraction, free-space length, and debris-space length, and demonstrated that free-space length exhibits the strongest independent correlation with wear performance across a broad range of polymer systems, while area fraction also retains significant predictive capability. These findings highlight both the value and the limitations of using individual morphological descriptors to represent transfer-film effects.

More recently, Ye *et al.* [22] proposed an asperity-adhesive-wear-based framework that bridges microscopic debris generation and macroscale transfer-film area fraction evolution. Their model describes transfer-film growth as a statistical outcome of debris generation, adhesion probability, and preferential load support by existing film, thereby establishing a direct link between asperity-scale adhesive events and macroscale wear reduction. This work provides an important mechanistic basis for understanding the role of transfer-film accumulation in wear evolution. However, the model by Ye et al. primarily describes the statistical evolution of transfer-film area fraction and does not explicitly account for the concurrent evolution of multiscale contact mechanics or the structural integrity of the transfer film, which are critical for predicting wear behavior in engineering sealing systems.

Despite these advances, existing studies either focus on identifying effective transfer-film descriptors or modeling the evolution of a single metric (e.g., area fraction), but do not explicitly couple multiscale rough-surface contact evolution with the changing structural state of the transfer film within a unified predictive framework. In reciprocating sealing systems such as composite piston rings in Stirling engines, wear evolution is governed not only by transfer-film coverage, but also by asperity deformation, film continuity, and internal compactness. This motivates the present study to integrate fractal contact descriptors with a composite transfer film index (TFI) that combines coverage, connectivity, and porosity, enabling a more comprehensive description of wear evolution from running-in to steady-state conditions. In addition, to distinguish model reconstruction from true forward prediction, the predictive capability of the proposed framework was further assessed by calibrating the parameter-evolution functions using only early-stage experimental data and validating the model against subsequently measured long-duration wear data, including newly added tests at 1920 min and 3000 min.

2. Establishment of the Contact Mechanics Model

2.1 Surface Roughness Characterization of the Piston

The rough contact surface of the piston ring exhibits pronounced fractal characteristics. Therefore, accurate characterization of the contact surface is a prerequisite for establishing a reliable wear prediction model. Previous studies [23] have shown that rough surface topography possesses self-affine and multiscale features. Based on fractal theory, a three-dimensional rough surface profile can be described using the Weierstrass-Mandelbrot (W-M) function [14]. In this study, the microscopic contact asperities on the rough surface are assumed to be isotropically distributed, and the corresponding bivariate surface height function can be derived as follows:

$$Z(x,y)=L\left(\frac{G}{L}\right)^{D-2}\left(\frac{\log_e\gamma}{M}\right)\sum_{m=1}^{M}\sum_{n=0}^{n_{\max}}\gamma^{(D-3)n}\cdot\left\{\cos\Phi_{m,n}-\cos\left[\frac{2\pi\gamma^{n}\left(x^{2}+y^{2}\right)^{1/2}}{L}\cdot\cos\left(\arctan(\frac{y}{x})-\frac{\pi m}{M}\right)+\Phi_{m,n}\right]\right\} \tag{1}$$

where Z(x, y) denotes the surface height of the rough profile, representing the amplitude of surface asperity fluctuations. D is the fractal dimension of the three-dimensional rough surface, with values ranging between 2 and 3. L represents the sealing length, which characterizes the geometric scale of the sealing interface. G is the characteristic scale parameter of the surface profile and is used to quantify the longitudinal roughness of the PTFE-based composite surface. The parameter $n$denotes the frequency index of the random profile and also corresponds to the asperity level. γ is the minimum cutoff frequency of the profile function (γ=1.5) [24]. $n_{\max}$ is the maximum frequency index associated with the cutoff length Ls [25]. $\Phi_{m,n}$ represents a random phase uniformly distributed in the interval (0, 2π).

Considering the severe operating conditions of Stirling engines, the interaction among asperities must be taken into account when establishing the fractal contact model of the piston ring interface. Accordingly, the following assumptions are adopted:

1. The contact surface of the piston ring is treated as a deformable rough surface.
2. The cylinder surface is assumed to be a rigid and smooth surface.
3. The influences of external disturbances and minor vibrations of the friction test apparatus during sliding are neglected.

Interactions among asperities on the rough surface induce additional deformation during contact. In this study, the effect of asperity-asperity interaction is characterized by an average height reduction, denoted by μ, which represents the decrease in the effective asperity height due to mutual interference, as illustrated in **Figure 1** The corresponding expression is given as follows:

$$\mu = 1.12\frac{\sqrt{F(P_n / A_a)}}{E} \tag{2}$$

where μ denotes the reduction in asperity height induced by asperity-asperity interactions, E is the elastic modulus of the piston ring material, P_n represents the contact load acting on the sealing interface, and A_a is the nominal contact area.

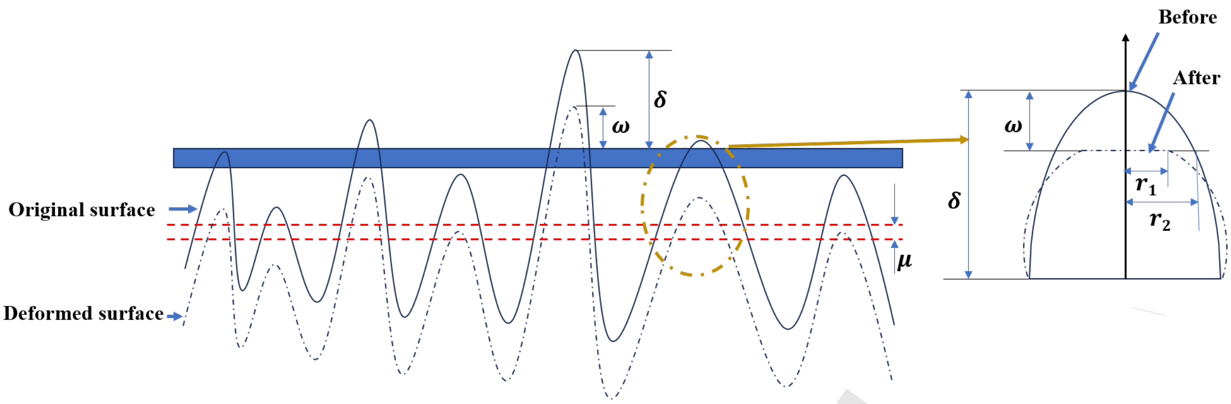

Figure 1 Schematic illustration of the microscopic contact between the rough piston ring surface and the rigid smooth cylinder surface, showing asperity deformation and the effect of asperity-asperity interactions on the effective contact state.

To simplify the theoretical model, the random phase $\Phi_{m,n}$ is set to zero, and the three-dimensional surface profile is reduced to a two-dimensional profile. Accordingly, the surface profile of an individual asperity prior to deformation can be expressed as:

$$Z(x) = G^{D-2} \left(\log_e \gamma\right)^{1/2} (2r)^{(3-D)} \left[\cos(\frac{\pi x}{r})\right] (-r_2 < x < r_2) \tag{3}$$

Accordingly, the maximum deformation of an individual asperity, denoted by δ, can be derived as:

$$Z(0) = \delta = G^{D-2} (\log_e \gamma)^{\frac{1}{2}} (2r)^{3-D} \tag{4}$$

Accordingly, the radius of curvature of an individual asperity can be obtained as:

$$R = \frac{(1+z'^2)^{\frac{3}{2}}}{z''}\Big|_{x=0} = \frac{a^{0.5D-0.5}}{2^{4-D} \pi^{1.5+0.5D} G^{D-2} (\log_e \gamma)^{\frac{1}{2}}} \tag{5}$$

The actual deformation of an individual asperity is given by:

$$\omega = \delta - \mu \tag{6}$$

2.2 Determination of Fractal Parameters

The surface profile of the piston ring was measured and sampled using a Super View W1 optical 3D surface profilometer with a sampling length of λ=1.52mm. The fractal dimension *D* and characteristic scale parameter *G* of the sealing surface were then evaluated. The structure function method is described as follows:

$$S(\tau) = CG^{2D-2}\tau^{4-2D} \tag{7}$$

$$C = \frac{\Gamma(2D-3)\sin\left[(2D-3)\pi/2\right]}{(4-2D)L\ln\gamma} \tag{8}$$

where, for a given value of *D, C* is a constant; Γ denotes the Euler gamma function; and *τ* represents an arbitrary increment of *x*. Taking the logarithm of both sides of Eq. (7) yields:

$$Lg\left[S(\tau)\right] = 2(D-1)LgG + LgC + (4-2D)Lg\tau \tag{9}$$

$$\begin{cases} D = \dfrac{4-k}{2} \\ G = \dfrac{b+\lg C}{2(D-1)} \end{cases} \tag{10}$$

where *k* and *b* are the slope and intercept, respectively, obtained from the least-squares linear fitting of the experimental data in the $\log_{10}S(\tau)$- lg(τ) plot. Therefore, the experimental data obtained from the three-dimensional surface profilometer were fitted to derive Eq. (10). As indicated by this equation, a linear relationship exists between lgS(τ) and lgτ, as illustrated in **Figure 2**. The slope and intercept of the linear fit were determined using the least-squares method. Based on Eq. (10), the fractal dimension *D* and characteristic scale parameter *G* of the PTFE-based composite at different wear stages were evaluated, and the results are summarized in **Table 1**.

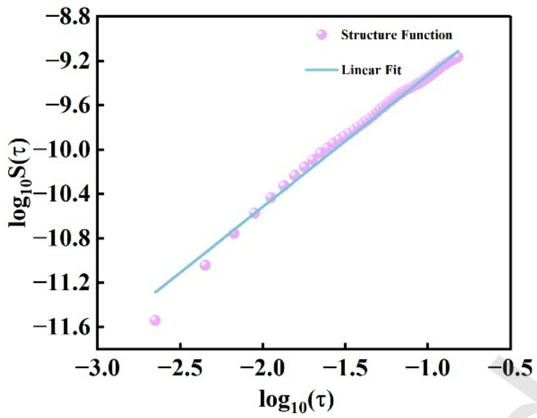

Figure 2 Determination of the fractal parameters of the piston ring surface at the initial wear stage based on the linear fitting relationship between $\log_{10}S(\tau)$ and $\lg(\tau)$, from which the fractal dimension *D* and characteristic scale parameter *G* are obtained.

Table 1(a) Fractal parameters of the piston ring surface at different stages (0-30 min)

Sample	Fractal parameter	Time/min				
		0	1	5	15	30
#1	D	2.4065	2.4788	2.5417	2.5918	2.6649
	$G(10^{-9}m)$	7.23	1.7	1.23	0.869	0.463

Table 1(b). Fractal parameters of the piston ring surface at different stages (60-960 min)

Sample	Fractal parameter	Time/min				
		60	120	240	480	960
#1	D	2.7842	2.865	2.9019	2.9038	2.905
	$G(10^{-9}m)$	0.045	0.0059	0.0026	0.0031	0.0013

The evolution of the fractal dimension *D* essentially characterizes the development and saturation of the complexity of multiscale surface roughness. Based on the trends summarized in **Table 1**, a saturation exponential model is adopted to fit the temporal evolution of $D(t)$:

$$D(t) = 2.901487 - 0.447157e^{-0.0227977t} \tag{11}$$

In the fractal theoretical framework, the characteristic scale parameter *G* reflects the amplitude of vertical height fluctuations of asperities. It decreases with increasing fractal dimension and prolonged sliding time. Accordingly, the temporal evolution of $G(t)$ is fitted as follows:

$$G(t) = 1.12 \times 10^{-12} + 7.25.53 \times 10^{-9} e^{-4.08t} + 1.7 \times 10^{-9} e^{-0.056t} \tag{12}$$

Figure 2. presents the fractal parameter determination procedure for the initial stage, while the results for other stages are given in **Appendix A**.

2.3 Relationship Between the Real Asperity Contact Area and the Contact Load

A contact model for individual asperities is established to relate the real contact area of the piston ring surface to the applied contact load. The asperity deformation behavior is described by explicitly considering three deformation regimes: the elastic regime, the elastoplastic regime, and the fully plastic regime. In particular, the elastoplastic regime is further divided into two sub-stages, namely the first and second elastoplastic deformation stages, to better capture the progressive transition of asperities from elastic deformation to complete plastic flow. Based on this framework, the real contact area and the corresponding contact load of the piston ring surface are calculated.

2.3.1 Elastic Deformation Regime

When $R >> \omega$, the asperity contact can be treated as a Hertzian contact. Accordingly, the relationship between the real contact area and the contact load is determined based on Hertz contact theory as follows:

$$a_e = \pi R \omega \tag{13}$$

$$F_e = \frac{4}{3} E R^{\frac{1}{2}} \omega^{\frac{3}{2}} \tag{14}$$

2.3.2 Elastoplastic Deformation Regime

Chang *et al.* [26] proposed a critical deformation area, denoted as ω_{ec}, which characterizes the transition of an asperity from the elastic deformation regime to the elastoplastic deformation regime.

$$w_{ec} = \left(\frac{\pi K H}{2E} \right)^2 R \tag{15}$$

Based on the model proposed by Kogut and Etsion (KE) [17], the elastoplastic deformation regime is further divided into the first and second elastoplastic deformation stages. For the first elastoplastic deformation stage, the contact area a_{epc1} and the corresponding contact load F_{epc1} are given by:

$$a_{epc1} = 0.93(\frac{w_{epc1}}{w_{ec}})^{1.136} a_{ec} \tag{16}$$

$$F_{epc1} = 1.373ER^{1/2}\omega_{ec}{}^{0.075}\omega^{1.425} \tag{17}$$

For the second elastoplastic deformation stage, the real contact area a_{epc2} and the corresponding contact load F_{epc2} are given by:

$$a_{epc2} = 0.94(\frac{w_{epc2}}{w_{ec}})a_{ec} \tag{18}$$

$$F_{epc1} = 1.867ER^{1/2}\omega_{ec}{}^{0.075}\omega^{1.425} \tag{19}$$

2.3.3 Fully Plastic Deformation Regime

As the contact load continues to increase, the real contact area expands, causing an increasing number of asperities to undergo fully plastic deformation. Under this condition, the real contact area a_{pc} and the corresponding contact load F_{pc} are expressed as follows:

$$a_{pc} = 2\pi R\omega \tag{20}$$

$$F_{pc} = 2\pi HR\omega \tag{21}$$

2.3.4 Relationship Between the Real Contact Area and the Contact Load for a Rough Surface

The real contact area and the applied contact load are critical parameters in the development of wear prediction models. Therefore, based on the above derivations and the modified Majumdar-Bhushan (M-B) model proposed in the literature [27], the relationship between the real contact area A_r and the applied contact load can be obtained by integrating the asperity area distribution function $n(a)$.

$$n(a) = \frac{D}{2}\psi^{\frac{2-D}{2}} a_l^{\frac{D}{2}} a^{\frac{-(D+2)}{2}} \tag{22}$$

When the maximum contact area of asperities a_l lies within the range $0 \le a_l \le a_{ec}$, all asperities are in the elastic deformation regime. When a_l falls within the interval $a_{ec} < a_l < a_{epc1}$, a portion of asperities undergo elastic deformation, while the remaining asperities enter the elastoplastic deformation regime. As a_l increases further to the range $a_{epc1} < a_l < a_{pc}$ the asperities exhibit a mixed deformation state, where some asperities remain elastic, others experience elastoplastic deformation, and the rest undergo fully plastic deformation. Based on these deformation distributions, the real contact load acting on the piston ring end face can be determined. When the maximum asperity contact area a_l exceeds a_{pc}, the asperity population simultaneously involves all three deformation regimes, namely elastic, elastoplastic, and fully plastic deformation.

$$F_n = \left\{ \begin{array}{c} \int_0^{a_{ec}} F_e n(a)da \Leftrightarrow 0 < a_l < a_{ec} \\ \int_0^{a_{ec}} F_e n(a)da + \int_{a_{ec}}^{a_{epc}} F_{ep1} n(a)da \Leftrightarrow a_{ec} < a_l < a_{epc} \\ \int_0^{a_{ec}} F_e n(a)da + \int_{a_{ec}}^{a_{epc}} F_{ep1} n(a)da + \int_{a_{epc}}^{a_{pc}} F_{ep2} n(a)da \Leftrightarrow a_{epc} < a_l < a_{pc} \\ \int_0^{a_{ec}} F_e n(a)da + \int_{a_{ec}}^{a_{epc}} F_{ep1} n(a)da + \int_{a_{epc}}^{a_{pc}} F_{ep2} n(a)da + \int_{a_{pc}}^{a_l} F_p n(a)da \Leftrightarrow a_{pc} < a_l \end{array} \right\} \tag{23}$$

$$A_r = \left\{ \begin{array}{c} \int_0^{a_{ec}} a_e n(a)da \Leftrightarrow 0 < a_l < a_{ec} \\ \int_0^{a_{ec}} a_e n(a)da + \int_{a_{ec}}^{a_{epc}} a_{ep1} n(a)da \Leftrightarrow a_{ec} < a_l < a_{epc} \\ \int_0^{a_{ec}} a_e n(a)da + \int_{a_{ec}}^{a_{epc}} a_{ep1} n(a)da + \int_{a_{epc}}^{a_{pc}} a_{ep2} n(a)da \Leftrightarrow a_{epc} < a_l < a_{pc} \\ \int_0^{a_{ec}} a_e n(a)da + \int_{a_{ec}}^{a_{epc}} a_{ep1} n(a)da + \int_{a_{epc}}^{a_{pc}} a_{ep2} n(a)da + \int_{a_{pc}}^{a_l} a_p n(a)da \Leftrightarrow a_{pc} < a_l \end{array} \right\} \tag{24}$$

The detailed equations corresponding to Section 2 are given in **Appendix B.**

2.4 Transfer Film Index (TFI)

During operation, the piston ring slides against the cylinder wall, and owing to the use of modified PTFE as the piston ring material, a transfer film is readily formed on the inner surface of the cylinder. The formation and evolution of the transfer film exert a crucial influence on the interfacial contact state and frictional behavior. The transfer film is primarily generated through the detachment of polymer material during sliding, followed by its adhesion, redeposition, compaction, and reconstruction on the counterface. Its morphology, thickness, and connectivity directly govern the real contact area, load distribution, wear mechanisms, and wear resistance of the material [28][29][30].

The transfer film is jointly characterized by its coverage, connectivity, and porosity, which together constitute a comprehensive evaluation index-referred to herein as the transfer film index (TFI) that governs the wear behavior of the material. The transfer film coverage C is defined as the ratio of the area covered by the piston ring material on the counterface to the total contact area, and represents the primary parameter describing the spatial distribution of the transfer film. To incorporate the actual morphological characteristics of the transfer film into the wear prediction model, a physical definition of the transfer film index (TFI) is established based on quantitative image analysis performed using MATLAB. The transfer film connectivity K reflects the intrinsic quality and structural stability of the film and serves as a key indicator of its structural compactness. The porosity H characterizes the film-forming quality within the covered regions and describes the extent of voids present in the transfer film.

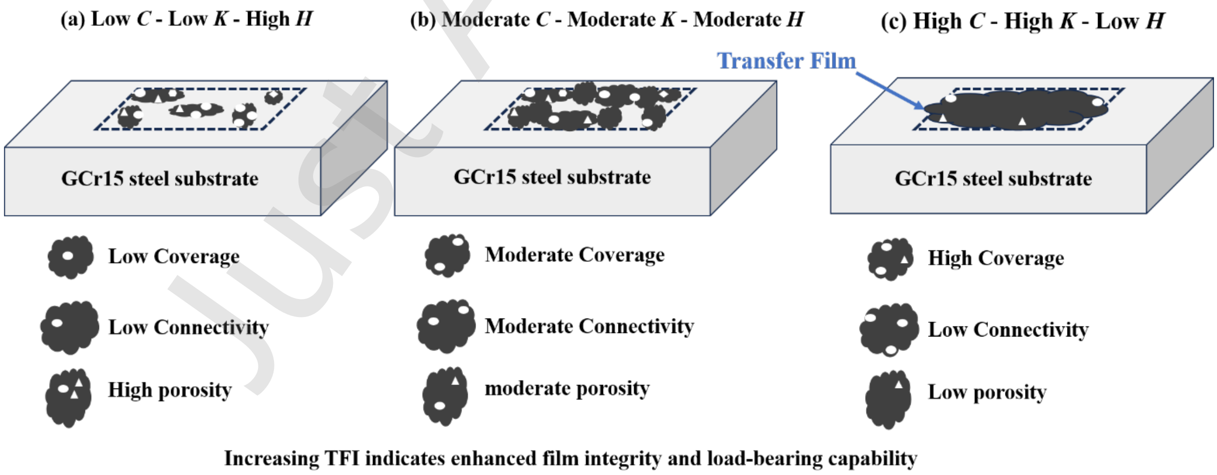

Figure 3 Conceptual schematic of transfer film evolution and the corresponding variations in morphological descriptors: (a) sparse and discontinuous transfer film at the initial stage, characterized by low coverage and connectivity and relatively high porosity; (b) partially connected transfer film

during the transition stage; (c) dense and continuous transfer film in the steady-state regime, with enhanced coverage, connectivity, and load-bearing capability.

To establish a statistically reliable formulation of the transfer film index (TFI), three parallel experiments were conducted at nine wear stages (1, 5, 15, 30, 60, 120, 240, 480, and 960 min), resulting in a total of 27 observations. Because the three descriptors exhibit different variation ranges, min–max normalization was first applied to eliminate scale effects. The detailed experimental data used in this analysis are provided in Appendix C (**Table C1**).

$$C^* = \frac{C - C_{\min}}{C_{\max} - C_{\min}},\quad K^* = \frac{K - K_{\min}}{K_{\max} - K_{\min}},\quad H^* = \frac{H - H_{\min}}{H_{\max} - H_{\min}} \tag{25}$$

For the present dataset,

$$C^* = \frac{C - 0.0352}{0.6628},\quad K^* = \frac{K - 0.0524}{0.9445},\quad H^* = \frac{H - 0.008}{0.0850} \tag{26}$$

A normalized inverse-wear-rate indicator was used as the regression target to evaluate the relative contributions of the transfer-film descriptors. The regression model is statistically significant overall (R^2=0.9748, adjusted R^2=0.9715, F=296.96, p=1.589×10^{-18}). The coefficient tests show that normalized coverage and normalized connectivity are statistically significant predictors, whereas normalized porosity exhibits weaker standalone significance under the present dataset.

After normalizing the absolute values of the regression coefficients, the weighting coefficients were obtained as:

$$\omega_C = 0.573,\quad \omega_K = 0.334,\quad \omega_H = 0.093 \tag{27}$$

Accordingly, the transfer film index was defined as:

$$TFI = 0.573C^* + 0.334K^* - 0.093H^* \tag{28}$$

This formulation indicates that transfer-film effectiveness is primarily governed by coverage and connectivity, while porosity acts as a negative correction term associated with film defects.

It should be noted that the regression coefficients and the final weighting coefficients are not identical quantities. The regression coefficients describe the marginal effects of the normalized descriptors on the response variable, whereas the weighting coefficients represent the relative contribution of each descriptor in the composite TFI formulation. Therefore, the weighting coefficients were obtained by normalizing the absolute values of the regression coefficients. Specifically, based on the regression coefficients 0.7589, 0.4425, and -0.1230, the corresponding weights were calculated as $\omega_C = 0.573$, $\omega_K = 0.334$, and $\omega_H = 0.093$. The negative sign of H^* was retained in the final formulation to reflect the detrimental effect of porosity on transfer-film integrity.

To verify the statistical validity of the TFI related weighting analysis, full regression diagnostics were performed using the 27 observation dataset. The regression model shows high explanatory capability and strong overall significance. The detailed regression results are summarized in Table 2. Coefficient tests indicate that normalized coverage (t=6.628, p=9.22×10^{-7}) and normalized connectivity (t=5.641, p=9.65×10^{-6}) are statistically significant contributors, whereas normalized porosity (t=-1.230, p=0.265) has weaker standalone significance. Therefore, the weighting analysis indicates that coverage and connectivity are the dominant contributors to the composite transfer-film index, while porosity provides a smaller negative correction.

Table 2 Regression results for normalized transfer-film descriptors

Term	Coefficient	Std. Error	t value	p value	95% CI
C^*	0.7589	0.1145	6.628	9.22×10^{-7}	[0.552, 0.996]
K^*	0.4425	0.0784	5.641	9.65×10^{-6}	[0.280, 0.605]
H^*	-0.1230	0.1076	-1.143	0.265	[-0.346, 0.10]

To achieve a more accurate characterization and measurement of the transfer film, image preprocessing was performed to enhance the contrast between the transfer film and the background. In this study, optical microscopy images of the transfer film were first converted into uniform grayscale images through preprocessing and flat-field correction. Considering that variations in illumination conditions and external factors during image acquisition may adversely affect threshold-based segmentation, Gaussian filtering was applied to suppress background intensity fluctuations, followed by flat-field correction. The corrected images were then linearly rescaled to an approximately intermediate gray-level range, thereby improving the stability of subsequent segmentation procedures.

On the flat-field-corrected images, intensity-based segmentation was carried out using the Otsu global thresholding method. Furthermore, to account for differences in relative background intensity among samples acquired at different wear stages, a polarity-based binary mask was constructed in which the transfer film and background were completely separated using distinct pixel values. To eliminate the influence of noise and fine debris on the final results, morphological closing followed by opening operations were applied to the binary mask, and small connected components were removed using an area threshold criterion. Subsequently, a consistent set of structural descriptors was calculated based on the refined mask, with a coverage range of 0.01-0.99 adopted as a validity criterion.

The averaged normalized TFI increases monotonically from 0.0427 at 1 min to 0.8083 at 960 min, indicating the progressive development of the transfer film from a sparse and discontinuous morphology to a dense and stable protective layer. A pronounced increase is observed after 60 min, and the TFI exceeds 0.70 at 240 min, corresponding to the onset of a stable low-wear regime.

Table 3 Transfer film parameters (coverage, connectivity, and porosity) at different wear stages

Time/min	C^{*}_{avg}	K^{*}_{avg}	H^{*}_{avg}	TFI
1	0.0329	0.0867	0.0549	0.0427
5	0.1103	0.0255	0.0627	0.0659
15	0.1883	0.0659	0.4549	0.0876
30	0.3120	0.1594	0.5294	0.1828
60	0.5004	0.0843	0.4863	0.2697
120	0.8066	0.4253	0.6745	0.5415
240	0.8808	0.8752	0.7765	0.7248
480	0.9213	0.9708	0.8941	0.7690
960	0.9925	0.9905	0.9804	0.8083

To investigate the temporal evolution of the transfer film index, an exponential saturation model is employed for fitting as follows:

$$TFI(t) = a\left(1 - e^{-t/b}\right) + C \tag{29}$$

$$TFI(t) = 0.7920\left(1 - e^{-t/122.82}\right) + 0.0160 \tag{30}$$

The fitting yields a coefficient of determination of R^2=0.9924, indicating that the exponential saturation model accurately captures the temporal evolution of TFI and its gradual stabilization with increasing time.

2.5 Establishment of the Wear Prediction Model

During reciprocating sliding, adhesive junctions are prone to form at the frictional contact interface between the piston ring and the cylinder wall, thereby inducing adhesive wear. This cyclic process of "adhesion-fracture-re-adhesion" leads to the continuous detachment of material fragments from the rough surface [31]. Owing to the enclosed configuration of the piston ring sealing structure, wear debris cannot be readily expelled, and the sealing interface is consequently subjected to additional abrasive wear. Therefore, in reconstructing a fractal-based wear model for the piston ring interface, both adhesive wear and abrasive wear mechanisms must be taken into account simultaneously. To quantify the wear contributions associated with these two mechanisms, a modified Archard wear theory is employed for analysis [32].

$$W = K_{\mathrm{e}} \frac{P}{\sigma_y} S \tag{31}$$

where W denotes the volumetric wear loss, K_e is the wear coefficient of the piston ring material, σ_y represents the yield stress of the piston ring material, and S is the sliding distance.

During operation, the piston ring and the cylinder wall form a tribological pair undergoing continuous sliding. Both normal and tangential stresses develop at the contact interface. Accordingly, based on the modified adhesion theory, the wear model can be expressed as follows [33]:

$$W = K_e \left(1 + \lambda f\right)^{1/2} A_r\left(D, G\right) S \tag{32}$$

where W denotes the volumetric wear loss of the piston ring, and K_{e1} is the effective wear coefficient. From a physical perspective, asperities on the rough contact surface may undergo elastic, elastoplastic, and fully plastic deformation during sliding. Accordingly, regime-dependent coefficients K_{e2}, K_{e3} [34]. However, due to the multiscale and mixed nature of rough-surface contact, their individual contributions cannot be directly separated or independently measured in the present experimental framework. Therefore, in the proposed model, their combined effect is represented by the effective coefficient K_e , which serves as an equivalent parameter characterizing the overall wear response of the contact interface. τ_b represents the shear yield stress of the piston ring material, f is the friction coefficient of the piston ring material, and A_r denotes the real contact area of the piston ring sealing surface under the applied contact load.

In this sense, K_e should be understood as a state-dependent equivalent parameter, rather than a fixed constant associated with a single asperity deformation regime.

To quantitatively describe the regulatory effect of the transfer film on contact behavior and wear resistance, a transfer film index is incorporated into the conventional contact model. The formation degree and protective capability of the transfer film are characterized using experimentally determined parameters, based on which a friction and wear prediction model is established as follows:

$$W = K_e\left(1+\lambda f\right)^{1/2} A_r\left(D(t),G(t)\right)S*\left(1-TFI(t)\right) \tag{33}$$

where F_{TFI} represents the transfer film factor. To account for the influence of transfer film evolution on wear behavior, TFI is incorporated into the wear model in a multiplicative form. Physically, the transfer film does not contribute directly to wear as an independent term; rather, it modifies the interfacial contact state by redistributing load, reducing direct asperity contact, and lowering interfacial shear resistance. Therefore, TFI is introduced as a regulating factor that proportionally modulates the wear response predicted by the contact mechanics framework. This multiplicative formulation reflects the coupled nature of contact deformation and transfer film evolution during sliding. This treatment is consistent with the general tribological modeling approach in which surface films act as modifying factors on effective contact conditions rather than independent wear sources. In this formulation, TFI is introduced as a dimensionless factor to represent the regulatory effect of the transfer film on interfacial wear behavior. Physically, the transfer film does not contribute independently to material removal; instead, it modifies the contact conditions by reducing direct asperity interaction, redistributing the applied load, and lowering the effective interfacial shear stress. Accordingly, TFI is incorporated in a multiplicative form to reflect its role as a contact-modulating factor. The linear expression (1 − TFI) is adopted as a first-order approximation, implying that the contribution of asperity-mediated wear decreases proportionally with the development of a more continuous and compact transfer film. This assumption provides a physically interpretable and parsimonious representation of the attenuation effect. It should be noted that alternative nonlinear forms, such as exponential or power-law relationships, could also be used to describe this effect. However, such formulations would introduce additional empirical parameters and require more extensive experimental validation. Therefore, the linear form is adopted in the present study as a reasonable first-order representation of the coupling between transfer film evolution and wear response. Normalizing the wear expression with respect to the applied load and sliding distance yields the volumetric wear rate W_r.

$$W_r = \frac{K_e\left(1+\lambda f\right)^{1/2} A_r\left(D(t),G(t)\right)*\left(1-TFI(t)\right)}{F} \tag{34}$$

3. Experiments and Characterization

3.1 Materials

As summarized in **Table 3**, the specific specifications and compositions of each constituent material used in the composite are provided, including polytetrafluoroethylene (PTFE), molybdenum disulfide (MoS_2), and tin bronze (CuSn10). Anhydrous ethanol (Tianjin Damao Chemical Reagent Factory) with a density of 0.791 g/cm^3 was used during the experimental procedures.

Table 4 Raw materials and their specifications

Raw materials	Specification	Sample manufacturer
PTFE	40 μm, M-111	Daikin Industries (Japan)
MoS_2	8000 mesh, MF-0	Shanghai Colloid Chemical Plant
CuSn10	150 μm, BRO-AW-3	Suzhou Futian High-Tech Powder Co., Ltd.

3.2 Sample preparation

The constituent materials were weighed and mixed according to the proportions listed in Table 3 Polytetrafluoroethylene (PTFE), tin bronze (CuSn10), and molybdenum disulfide (MoS_2) were blended at a mass ratio of 8:11:1 using a high-speed mixer. To ensure uniform dispersion, the mixing process was repeated five times. The resulting powder mixture was subsequently sieved through a 45-mesh screen to remove large agglomerates. The sieved mixture was then uniformly loaded into a mold and compacted under a pressure of 55 MPa. After maintaining the applied pressure for 5 min, the green compact was demolded and trimmed to remove burrs. Following a resting period of 24 h, the specimens were placed in a sintering furnace and heated from room temperature to 370 °C at a rate of 60 °C h^{-1}. The samples were held at 370 °C for 3 h and then allowed to cool naturally to room temperature. The preparation procedure is illustrated in **Figure 4** The measured properties of the composite materials are summarized in **Table 4.**

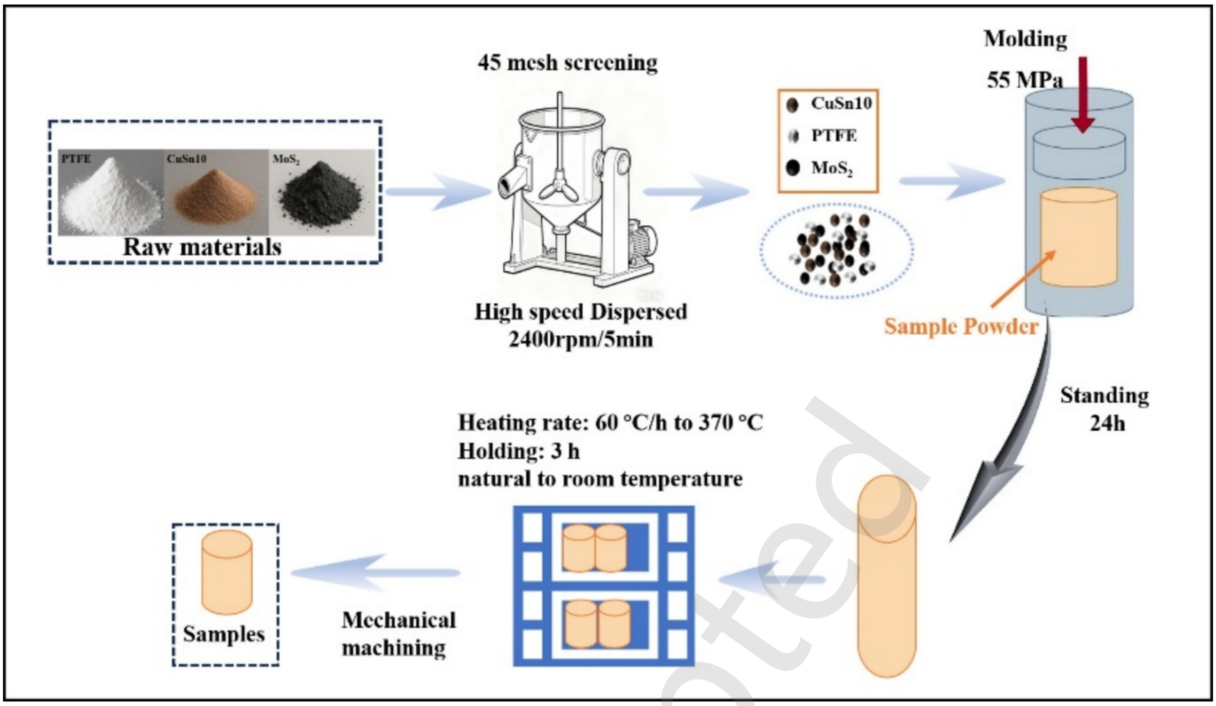

Figure 4 Preparation procedure of the modified PTFE-based composite piston ring material, including mixing, sieving, cold pressing, demolding, resting, and sintering .

Table 5 Properties of the piston ring material

materials	Elasticity modulus(MPa)	shear elasticity(GPa)	Poisson's ratio	Density(g/cm^3)
modified PTFE	928	0.11	0.34	3.9

3.3 Experimental Procedure

To investigate the tribological behavior of PTFE-based composite materials, friction and wear tests were conducted using a linear reciprocating tribometer (model LSM-200, Lanzhou Zhongke Huake Technology Co., Ltd.). The structure and operating principle of the test apparatus are illustrated in **Figure 5**. Prior to testing, the friction surface of the specimen and the mating metallic counterface were cleaned with cotton swabs soaked in anhydrous ethanol to remove surface contaminants and ensure a clean contact interface. The specimen was then mounted on the loading holder, and a normal pressure of 3.5 MPa was applied. During the tests, the sliding linear velocity was maintained at approximately 80 mm/s, and the ambient temperature was controlled at 25 °C. All experiments were performed under room-temperature conditions, with relative motion between the friction pair achieved through linear reciprocating sliding. After completion of the tests, the wear tracks were examined and analyzed to evaluate the friction coefficient and wear resistance of the materials. To capture the evolution of tribological behavior, the friction process was divided into eleven time intervals: 1, 5, 15, 30, 60, 120, 240, 480, 960, 1920, and 3000 min. At each interval, the friction coefficient, volumetric wear rate, and transfer film coverage were evaluated. The specimens were weighed to determine the mass loss, and the average volumetric wear rate W_r at each stage was calculated according to Eq. (35).

$$W_r = \frac{\Delta m}{\rho N L} \tag{35}$$

where Δm denotes the mass loss of the specimen before and after testing (g), ρ is the density of the specimen material (g/cm^3), N represents the load applied to the specimen end face, and L is the total sliding distance. The data at 1920 min and 3000 min were additionally introduced to provide an extended-time validation of the proposed model and to examine its forward predictive capability beyond the original experimental range.

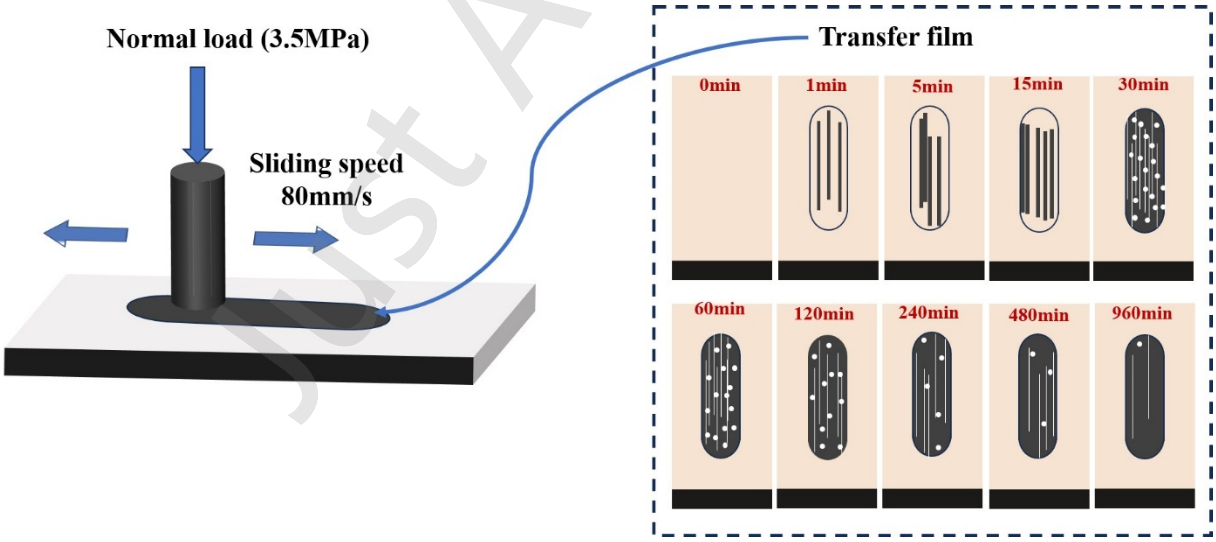

Figure 5 Schematic diagram of the reciprocating friction and wear test setup used to evaluate the tribological behavior of the piston ring material under dry sliding conditions.

3.4 Transfer Film Image Processing

After completion of the friction tests, high-resolution images of the transfer film formed on the counterface were captured using an optical microscope (Axio Imager M2m, Zeiss, Jena, Germany). To minimize the influence of local heterogeneity on the statistical results, three to five fields of view were randomly selected within the wear track of each specimen, and the averaged values were taken as the final results. The microscopic morphologies of the transfer film obtained at different sliding times (1, 5, 15, 30, 60, 120, 240, 480, and 960 min) are shown in **Figure 6**. With increasing sliding time, pronounced variations in the coverage and connectivity of the transfer film on the wear track surface can be observed. To enable quantitative identification of the transfer film regions and calculation of their area fractions, digital image processing was performed on the original micrographs using MATLAB software. This procedure was employed to enhance the contrast between the transfer film and the substrate and to extract relevant morphological parameters [35].

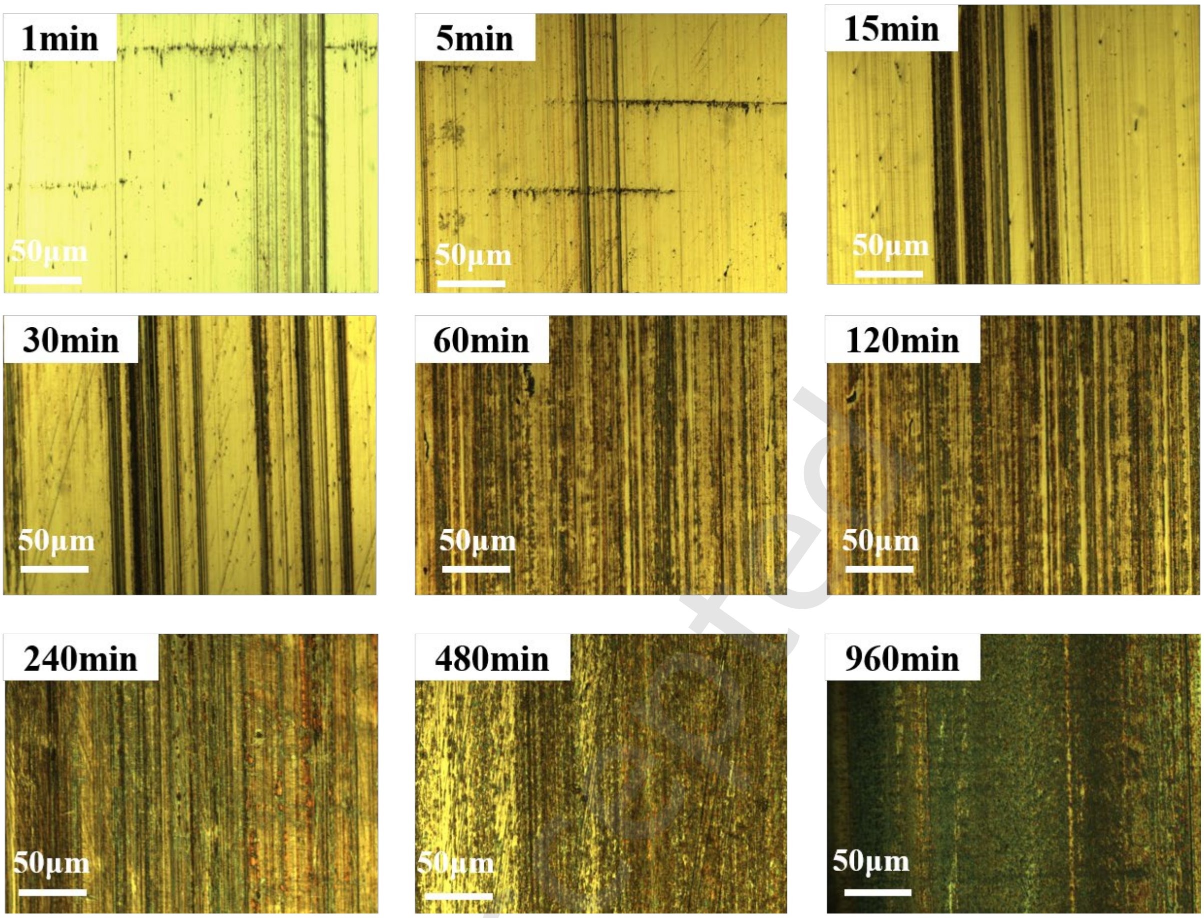

Figure 6 Optical micrographs of transfer films formed on the counterface at different sliding times, showing the progressive evolution from isolated and discontinuous patches to a dense and continuous transfer film.

First, the color micrographs were converted into grayscale images. Then, grayscale enhancement and flat-field correction were applied to mitigate the effects of non-uniform illumination. This step effectively improves the grayscale contrast between the transfer film regions and the substrate. Subsequently, the Otsu global thresholding algorithm was employed to automatically binarize the images, avoiding subjective errors associated with manual threshold selection. Then, we processed the resulting binary images with morphological operations. These operations helped remove noise and enhance region connectivity. In this way, we obtained binary representations that precisely show the transfer film's spatial distribution. Finally, we calculated the transfer film coverage. The calculation was done by finding the ratio of transfer film region pixels to the total pixels in the wear track area.

This metric was used to quantitatively analyze the formation and evolution of the transfer film at different sliding times. The detailed image processing workflow is illustrated in **Figure 7** (taking the 5 min sliding condition as an example), while the processing procedures for other time intervals are provided in **Appendix D.**

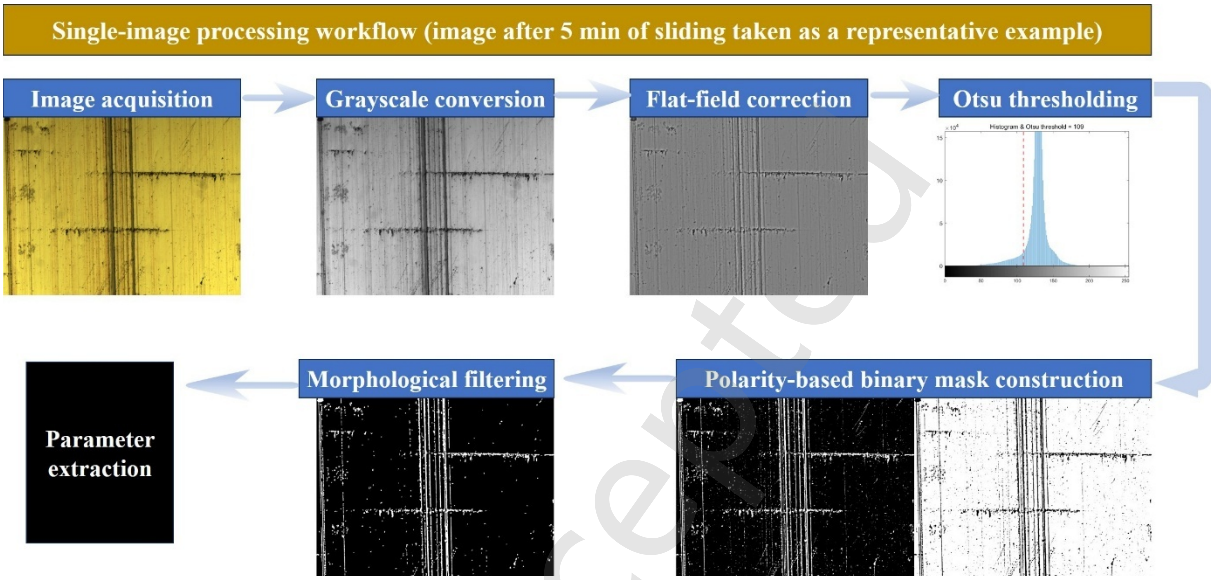

Figure 7 Image processing workflow used for quantitative characterization of the transfer film, taking the micrograph obtained after 5 min of sliding as a representative example, including grayscale conversion, flat-field correction, threshold segmentation, morphological processing, and parameter extraction.

4. Results and Discussion

Compared with existing fractal wear models, which primarily focus on asperity deformation mechanisms, the present work incorporates the dynamic evolution of transfer films into the wear prediction framework. Meanwhile, unlike transfer film characterization studies, which remain descriptive, the proposed TFI is directly embedded into the wear model as a governing variable. Therefore, the key novelty of this work lies not in the individual components, but in establishing a physically coupled mechanism that links multiscale contact mechanics with evolving interfacial lubrication conditions.

4.1 Evaluation of Fractal Parameter Fitting

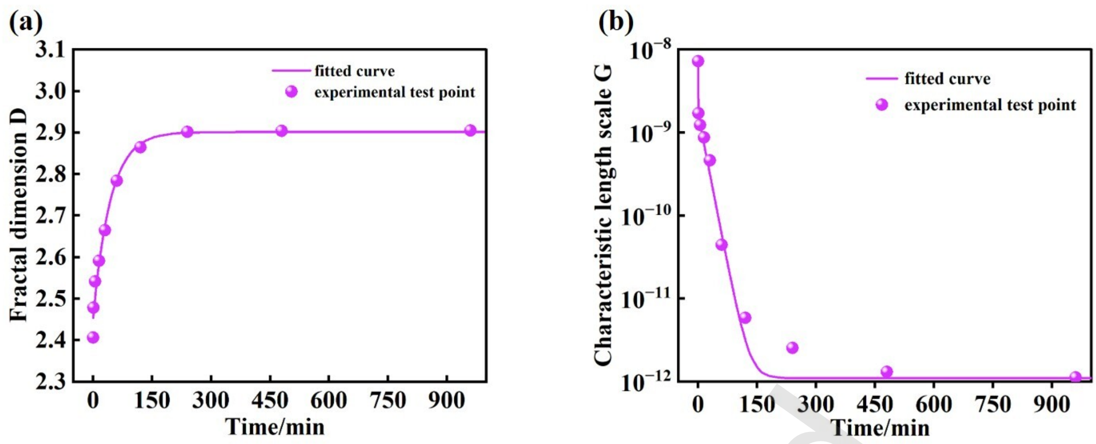

Figure 8 Fitting results of the time-dependent fractal parameters of the piston ring surface: (a) evolution and exponential fitting of the fractal dimension *D*; (b) evolution and fitting of the characteristic scale parameter *G*.

Fractal dimension *D* and characteristic scale parameter *G* are core indicators reflecting the evolution of piston ring surface roughness during wear. As shown in Figure 8, the exponential model fits the temporal evolution of *D* with a high coefficient of determination ($R^2 = 0.987$), which accurately captures the rapid increase in surface complexity in the early friction stage and subsequent stabilization. This trend directly corresponds to the transition from the running-in stage to the quasi-steady wear regime: initial sliding causes continuous wear of surface asperities, which increases the complexity of the multiscale roughness structure. As the wear process progresses, the surface topography gradually reaches dynamic equilibrium, leading to saturated *D* values. For the characteristic scale parameter *G* ($R^2 = 0.932$), the proposed bi-exponential function reliably describes its temporal evolution despite a dynamic range spanning several orders of magnitude. Compared with the fitting quality of *D*, the relatively lower R^2 value of *G* is mainly due to its high sensitivity to the initial surface state. Rapid material removal in the early sliding stage causes drastic changes in the vertical height fluctuations of asperities, resulting in greater variability in *G* data. The continuous decrease in *G* from 7.23×10^{-9} m to 1.3×10^{-12} m further confirms that the piston ring surface gradually becomes smooth as wear progresses, which is consistent with the experimental observation of reduced surface roughness.

4.2 Correlation Analysis between Morphological Parameters and Wear Indicators

The wear rate and friction coefficient of the piston ring specimen exhibit distinct stage-dependent characteristics with increasing sliding time (**Figure 9(a)**). In the initial friction stage (0-30 min), no effective protective transfer film forms on the surface, and the tribological pair is dominated by direct asperity contact. This leads to a high wear rate (up to the order of 10^{-4}) and friction coefficient (initial value 0.261). As a small amount of transfer film begins to form on the counterface, the wear rate gradually decreases to the order of 10^{-5}.

In the intermediate friction stage (60-120 min), the wear rate further drops to the order of 10^{-6}, indicating the onset of the low-wear regime. At this stage, the initial transfer film forms locally on the counterface, but the film structure still contains numerous pores and exhibits limited connectivity, resulting in insufficient substrate protection. In the stable friction stage (240-960 min), the transfer film coverage continues to expand and becomes increasingly interconnected. The connectivity and compactness of the film are significantly enhanced, while the number of pores is markedly reduced. The formation of a continuous transfer film effectively isolates direct contact between the tribological pair, leading to a substantial reduction in both wear rate and friction coefficient. The friction coefficient fluctuates slightly around 0.173 and remains stable, reflecting the stable lubrication effect of the mature transfer film.

Figure 9(b) quantitatively presents the temporal evolution of transfer film coverage, connectivity, and porosity. In the initial stage, coverage and connectivity are relatively low (coverage < 0.2, connectivity < 0.16), while porosity is high ($\approx$0.019-0.056), indicating the transfer film is distributed in a discontinuous island-like morphology and provides limited protection to the substrate surface. As sliding progresses, coverage increases from below 0.2 to approximately 0.7, connectivity rises sharply from 0.404 at 120 min to 0.963 at 240 min, and porosity decreases continuously. This evolution reflects the gradual transition of the transfer film from a discontinuous, porous structure to a dense, continuous morphology. Notably, after approximately 120 min, the variation range of these parameters narrows, suggesting the transfer film enters a stable growth stage.

The transfer film index (TFI), integrating coverage, connectivity, and porosity, provides a comprehensive evaluation of film quality. As shown in **Figure 9(c)**, TFI exhibits a monotonic increasing trend with time, rising from an initial 0.0427 to 0.808 at 960 min, which confirms continuous improvements in transfer film integrity and load-bearing capacity. Correspondingly, **Figure 9**(d) shows the friction coefficient gradually decreases with increasing TFI, presenting a pronounced negative linear correlation ($R^2 \approx 0.91$). This consistency demonstrates that the formation of a continuous, compact transfer film effectively suppresses direct asperity contact at the friction interface, reduces interfacial shear resistance, and thus improves tribological performance.

A key finding from our experiments is that when TFI ≥ 0.7 (achieved at 240 min), the material enters a stable low-wear regime. At this threshold, the transfer film connectivity reaches ≥0.963, forming a dense and continuous protective layer that fully dominates the interfacial load-bearing and lubrication processes. This result clarifies the core mechanism of wear reduction: the transition from asperity-dominated contact to transfer-film-controlled shear, which provides a measurable criterion for assessing the service status of piston rings.

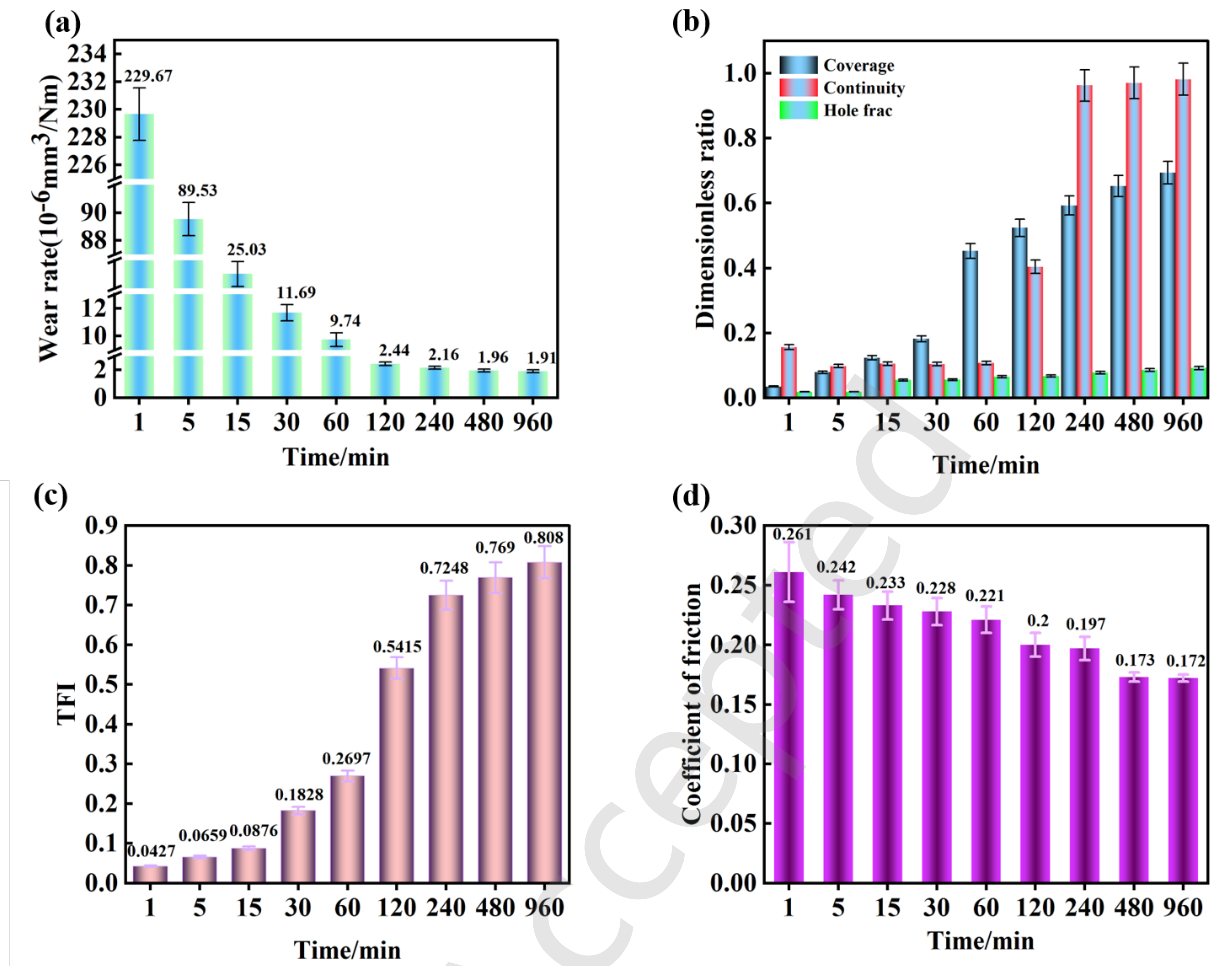

Figure 9 Evolution of tribological parameters and transfer film characteristics with sliding time: (a) wear rate; (b) transfer film coverage, connectivity, and porosity; (c) temporal evolution of the transfer film index (TFI); (d) friction coefficient.

4.3 Error Analysis between the Predicted Model and Experimental Measurements

To verify the validity of the modified wear model given in Eq. (33), the real contact are $A_r(D, G)$ was calculated based on the fractal dimension D and the characteristic scale parameter G. By further incorporating the friction coefficient f and the TFI, the predicted volumetric wear rate W_r^{pred} was obtained. The predicted results were then compared point by point with the experimentally measured wear rate W_r^{exp}, as shown in **Figure 10.**

In the revised analysis, it is important to distinguish between the reconstruction capability of the model and its forward predictive capability. Therefore, two complementary validation strategies were employed. First, the full-period dataset was used to evaluate whether the proposed framework can consistently reproduce the complete wear-evolution process. Second, to assess the true predictive significance of the model, a forward-validation scheme was introduced, in which only early-stage experimental data were used for parameter calibration, while subsequent wear behavior was predicted without including later-stage data in the fitting process.

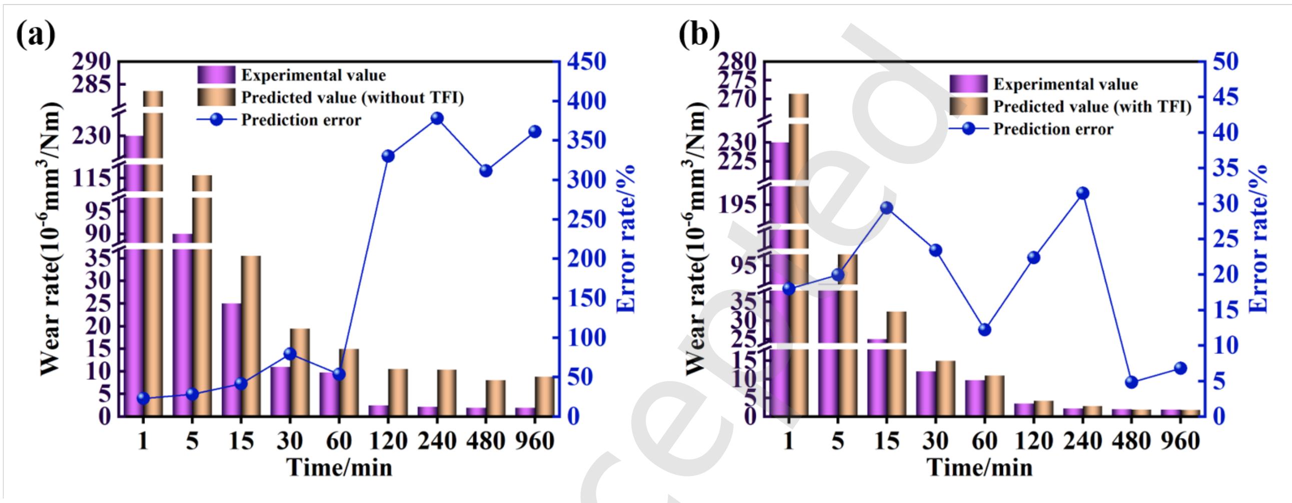

Figure 10 Comparison of predicted and experimental volumetric wear rates under different sliding durations: (a) experimental wear rates versus the values predicted by the proposed wear model with the transfer film index (TFI) incorporated; (b) comparison between model predictions without and with TFI, illustrating the enhancement in prediction accuracy achieved by considering transfer film evolution.

(1) Comparison between Predicted and Experimental Results

As shown in **Figure 10(a)**, the wear rates predicted by the proposed model exhibit good agreement with the experimental measurements in terms of both magnitude and temporal evolution. During the running-in stage (1-30 min), both the predicted and experimental wear rates remain at relatively high levels and display a rapid decreasing trend with increasing sliding time, which is consistent with the experimentally observed behavior. In the intermediate wear stage (30-120 min), the predicted values closely follow the variation trend of the experimental data, indicating that the modified model is capable of effectively capturing the influence of transfer film formation on the wear rate. When the sliding time exceeds 120 min, both the predicted and experimental wear rates enter a steady-state regime and converge to the order of 10^{-6}. These results demonstrate that the proposed wear prediction model exhibits a high level of reliability under the tested conditions.

(2) Improvement in Prediction Accuracy after Incorporating the Transfer Film Index (TFI)

To evaluate the effect of incorporating the TFI, the predictions obtained from the model without TFI were compared with the experimental measurements. As shown in **Figure 10(b)**, during the running-in stage, the predicted wear rates are close to the experimental values. This is mainly attributed to the limited formation of the transfer film at the early stage, where only slight wear scars are present and the influence of the transfer film on the overall wear rate remains negligible. However, during the later stages of the running-in period and the steady-state wear regime, models relying solely on the fractal dimension and characteristic scale parameter fail to explain the rapid decrease in wear rate. After 60 min of sliding, the predicted wear rates obtained without considering TFI are significantly higher than the experimental values by approximately a factor of 2-3. This discrepancy arises because conventional models implicitly assume direct contact between the mating surfaces and neglect both the load-bearing capacity of the transfer film and its wear-reducing effect during sliding.

When the TFI in the model is replaced by the experimentally determined values obtained through MATLAB-based image analysis, the prediction accuracy is substantially improved. In the intermediate wear stage, the predicted wear rates closely overlap with the experimental results. In the steady-state wear regime, as shown in **Figure 10**, both the predicted and experimental wear rates stabilize at the order of 10^{-6}, and the prediction error is markedly reduced. Compared with the original model, the relative error decreases from 23.26~378.24% to 4.85~31.48%. These results clearly demonstrate that the incorporation of TFI is a key factor in improving the accuracy of wear rate prediction.

(3) Evaluation of the Goodness of Fit (R^2)

The coefficient of determination (R^2) is calculated using the experimentally measured wear rate W_r^{exp} and the model-predicted wear rate W_r^{pred} to quantitatively evaluate the goodness of fit of the proposed wear prediction model:

$$R^2 = 1 - \frac{\sum \left(W_r^{\exp} - W_r^{pred} \right)^2}{\sum \left(W_r^{\exp} - \overline{W_r^{\exp}} \right)^2} \tag{36}$$

Without incorporating the transfer film index (TFI), the coefficient of determination is approximately R^2 = 0.9149. After introducing TFI, the value increases to R^2 = 0.9545, indicating a substantial improvement in the prediction accuracy of the model. This enhancement demonstrates that the inclusion of TFI enables the wear prediction model to evolve from a coarse trend-based estimation to an effective tool for quantitative prediction. Overall, the predicted results show close agreement with the experimental data. Nevertheless, local deviations between the predicted and experimental values still exist. These discrepancies primarily originate from the dynamic fluctuations associated with transfer film formation, including intermittent film detachment and regeneration during sliding. In addition, uncertainties arising from the extraction of transfer film coverage, connectivity, and porosity partly due to image processing and manual intervention also contribute to the prediction error. Such deviations are mainly concentrated in the intermediate wear stage, where the transfer film structure is still evolving. In contrast, during the later stages, the transfer film gradually stabilizes, leading to improved fitting accuracy and more reliable wear predictions.

(4) Forward Prediction and Extended-Time Validation

To further evaluate whether the proposed framework possesses genuine predictive capability rather than only post hoc fitting performance, a forward-validation scheme based on partial early-stage data was carried out. Specifically, only the early-stage experimental data were used to calibrate the temporal evolution functions of the fractal parameters *D*(*t*), *G*(*t*), and the transfer film index *TFI*(*t*). The calibrated model was then extrapolated to predict the wear behavior at later stages that were not involved in the parameter identification process.

In addition, to provide a more stringent validation, new long-duration experiments were conducted at 1920 min and 3000 min. These data points were not included in the model calibration and were used exclusively for extended-time validation. As shown in **Table 6**, the predicted wear rates at these two time points show good agreement with the corresponding experimental measurements, with errors of 6.22% and 7.29%. The predicted wear rates at these two time points show good agreement with the corresponding experimental measurements, indicating that the model is capable of capturing the long-term evolution trend of wear behavior beyond the original experimental range. In particular, the model successfully reproduces the sustained low-wear regime and reflects the continued dominance of transfer-film-controlled lubrication at prolonged sliding durations. This demonstrates that the proposed framework is not limited to reconstructing existing data, but retains meaningful forward predictive capability for long-term wear evolution and lifetime assessment.

Nevertheless, some deviations at extended durations are inevitable due to cumulative uncertainties in extrapolating transfer film evolution and the stochastic nature of film rupture and regeneration processes. Despite these uncertainties, the overall prediction trend remains consistent with experimental observations, confirming the robustness and engineering applicability of the model.

Table 6 Forward Prediction Performance: Comparison Between Predicted and Experimental Wear Rates at Extended Durations

Time/min	W (Predicted)	W (Experimental)	Error (%)
1920	1.827	1.72	6.22%
3000	1.82	1.69	7.29%

It should be noted that the present model is validated based on a PTFE-based composite system under a single set of controlled room-temperature conditions (25 °C, 3.5 MPa, 80 mm/s), which primarily serves as a baseline scenario to isolate the fundamental mechanisms governing wear evolution and transfer film formation. In practical Stirling engine applications, however, piston rings are subjected to more complex operating environments, including variable temperatures, fluctuating loads, and diverse material combinations.

To further clarify the scope and applicability of the proposed model, the following points should be noted. Despite these constraints, the proposed framework is established on general physical mechanisms, namely multiscale rough surface contact and interfacial transfer film evolution. The model parameters, including fractal descriptors (D, G) and the transfer film index (TFI), possess clear physical meanings and are expected to evolve with both operating conditions and material properties. Therefore, the framework is inherently adaptable to other tribological systems exhibiting similar transfer-film-dominated wear behavior. Nevertheless, the current validation is limited to a specific material system and operating condition, which may constrain its direct applicability to more complex engineering scenarios. Future work will focus on extending experimental validation to variable temperature and load conditions, as well as to different material systems, in order to further assess the robustness and general applicability of the proposed model.

5. Conclusions

1. A unified wear prediction framework is developed by integrating fractal contact mechanics with transfer film evolution. The model captures the full transition from asperity-dominated contact during the running-in stage to transfer-film-controlled lubrication in the steady-state regime.
2. A composite transfer film index (TFI) is proposed by integrating coverage, connectivity, and porosity with statistically derived weights (ω_C = 0.573, ω_k = 0.334, ω_H = 0.093). The TFI increases from 0.0427 to 0.8083, quantitatively characterizing the progressive formation of a dense and continuous transfer film.
3. A strong negative correlation ($R^2 \approx 0.91$) is observed between TFI and the friction coefficient. When TFI ≥ 0.7, the system enters a stable low-wear regime, indicating that the transfer film becomes the dominant load-bearing and lubrication mechanism.

4. Incorporating TFI significantly improves prediction accuracy, with R^2 increasing from approximately 0.9149 to 0.9545 and the relative error reduced to 4.85~31.48%. The model successfully captures the complete wear evolution process and demonstrates reliable forward predictive capability for extended operating durations.

Appendix

A. Processing of Fractal Dimension Data

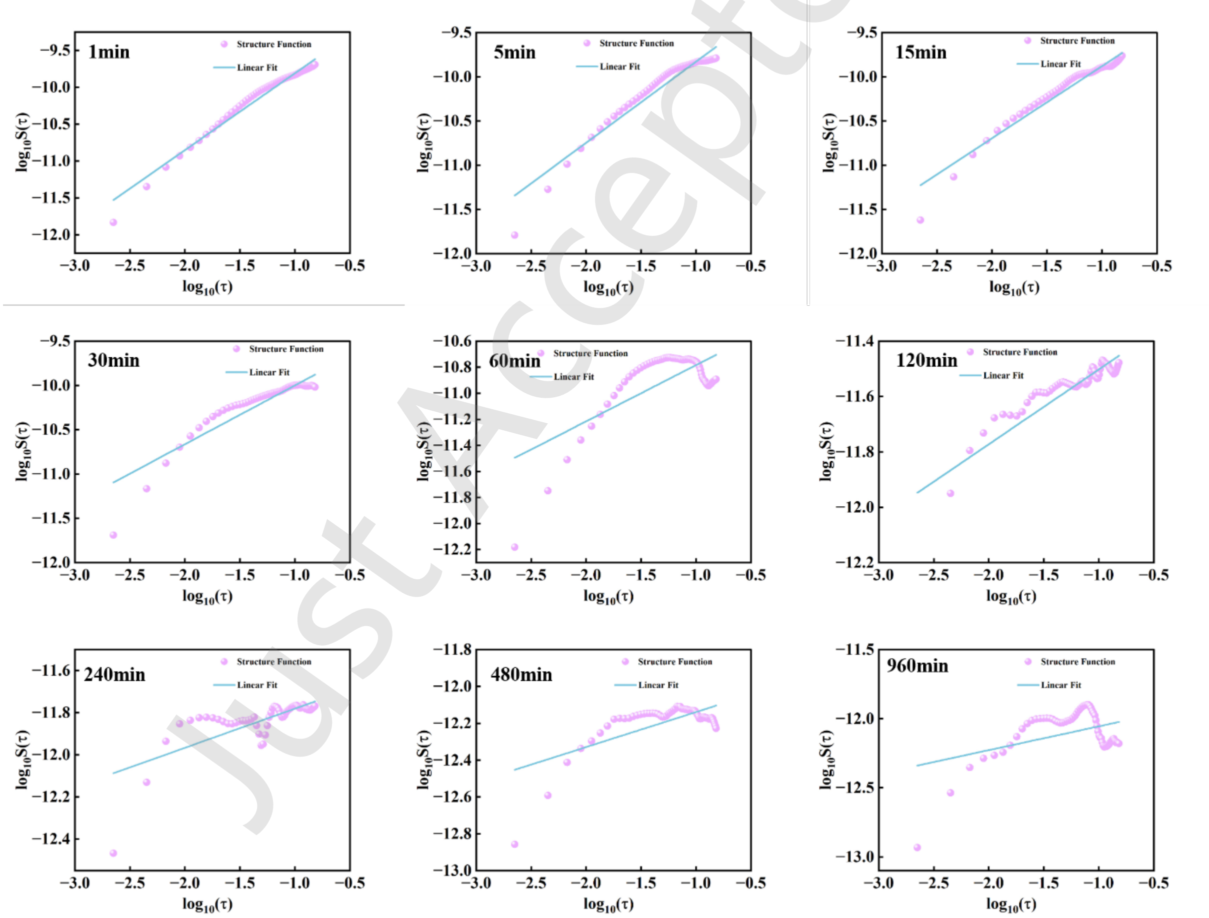

B. Other relevant equations used in the model calculations

$$b_1 = 2^{4-D}\pi^{0.5D-1.5}G^{(D-2)}(\log_e\gamma)^{1/2};\quad b_2 = \left[2^{4-D}\pi^{1.5+0.5D}G^{(D-2)}(\log_e\gamma)^{1/2}\right]^{-1};$$
$$b_3 = 1.12E(\frac{F_n}{A_a})^{0.5}; b_4 = b_2\left(\frac{\pi K\phi}{2}\right)^2; a_{ec} = (\frac{b_4 + b_3 b_2}{b_1})^{\frac{1}{2-D}} \quad \text{(B1)}$$

$$w_e = b_1 a^{1.5-0.5D} - b_3\left[(\frac{4}{3}E)^{0.5} b_2^{0.25} a^{0.125D-0.125} w_e^{0.75} + \sigma^{0.5}\pi^{0.5} b_2^{0.5} a^{0.25D-0.25} w_e^{0.5}\right] \quad \text{(B2)}$$

$$w_{ec} = \left(\frac{\pi KH}{2E}\right)^2 R = \left(\frac{\pi KH}{2E}\right)^2 b_2 a^{0.5D-0.5} = b_4 * a^{0.5D-0.5} \quad \text{(B3)}$$

$$w_{ep1} = b_1 a^{1.5-0.5D} - b_3\left[(1.373E)^{0.5} b_2^{0.25} b_4^{0.0375} a^{0.14375D-0.14375} w_{ep1}^{0.7125}\right] \quad \text{(B4)}$$

$$w_{ep2} = b_1 a^{1.5-0.5D} - b_3\left[(1.867E)^{0.5} b_2^{0.25} b_4^{0.1185} a^{0.18425D-0.18425} w_{ep2}^{0.6315}\right] \quad \text{(B5)}$$

$$w_p = b_1 a^{1.5-0.5D} - 2^{0.5}\pi^{0.5} b_3 b_2^{0.5} a^{0.25D-0.25} \quad \text{(B6)}$$

$$\begin{aligned}
A_e &= 0.5(D-1)\pi b_2 \varphi^{1.5-0.5D} a_l^{0.5D-0.5}\int_0^{a_{ec}} a^{-1} w_e da \\
A_{ep1} &= 0.465(D-1) b_4^{-1.136}\varphi^{1.5-0.5D} a_{ec} a_l^{0.5D-0.5}\int_{a_{ec}}^{a_{epc}} a^{0.068-1.068D} w_{ep1} da \\
A_{ep2} &= 0.47(D-1) b_4^{-1.146}\varphi^{1.5-0.5D} a_{ec} a_l^{0.5D-0.5}\int_{a_{epc}}^{a_{pc}} a^{0.073-1.073D} w_{ep2} da \\
A_p &= \pi b_2 \varphi^{1.5-0.5D} a_l^{0.5D-0.5}\int_{a_{pc}}^{a_l} a^{-1} w_p da
\end{aligned} \quad \text{(B7)}$$

C. The complete dataset used for the weighting analysis is provided in this appendix to improve transparency and reproducibility. The dataset contains 27 observations obtained from three parallel experiments across nine wear stages.

Table C1. Dataset used for the weighting analysis of normalized transfer-film descriptors

t/min		C	K	H	W_r
1	①	0.0352	0.156	0.019	250
	②	0.0668	0.121	0.011	225
	③	0.069	0.126	0.008	214
5	①	0.079	0.098	0.019	94.6
	②	0.1335	0.0524	0.008	85
	③	0.1125	0.079	0.013	89
15	①	0.124	0.105	0.055	28.1
	②	0.18	0.124	0.042	25
	③	0.176	0.115	0.043	23

30	①	0.182	0.104	0.056	14.7
	②	0.244	0.21	0.051	10.9
	③	0.30	0.295	0.052	9.46
60	①	0.453	0.108	0.065	9.82
	②	0.3156	0.125	0.042	9.63
	③	0.332	0.163	0.041	9.76
120	①	0.524	0.404	0.067	2.81
	②	0.583	0.460	0.064	2.35
	③	0.6024	0.4984	0.065	2.17
240	①	0.593	0.963	0.078	2.21
	②	0.6305	0.896	0.075	2.12
	③	0.6335	0.778	0.069	2.15
480	①	0.653	0.971	0.086	1.93
	②	0.6417	0.964	0.084	2.01
	③	0.6428	0.9731	0.082	1.95
960	①	0.694	0.982	0.092	1.91
	②	0.698	0.9969	0.093	1.87
	③	0.687	0.985	0.089	1.95

D. Raw optical micrographs at different wear stages

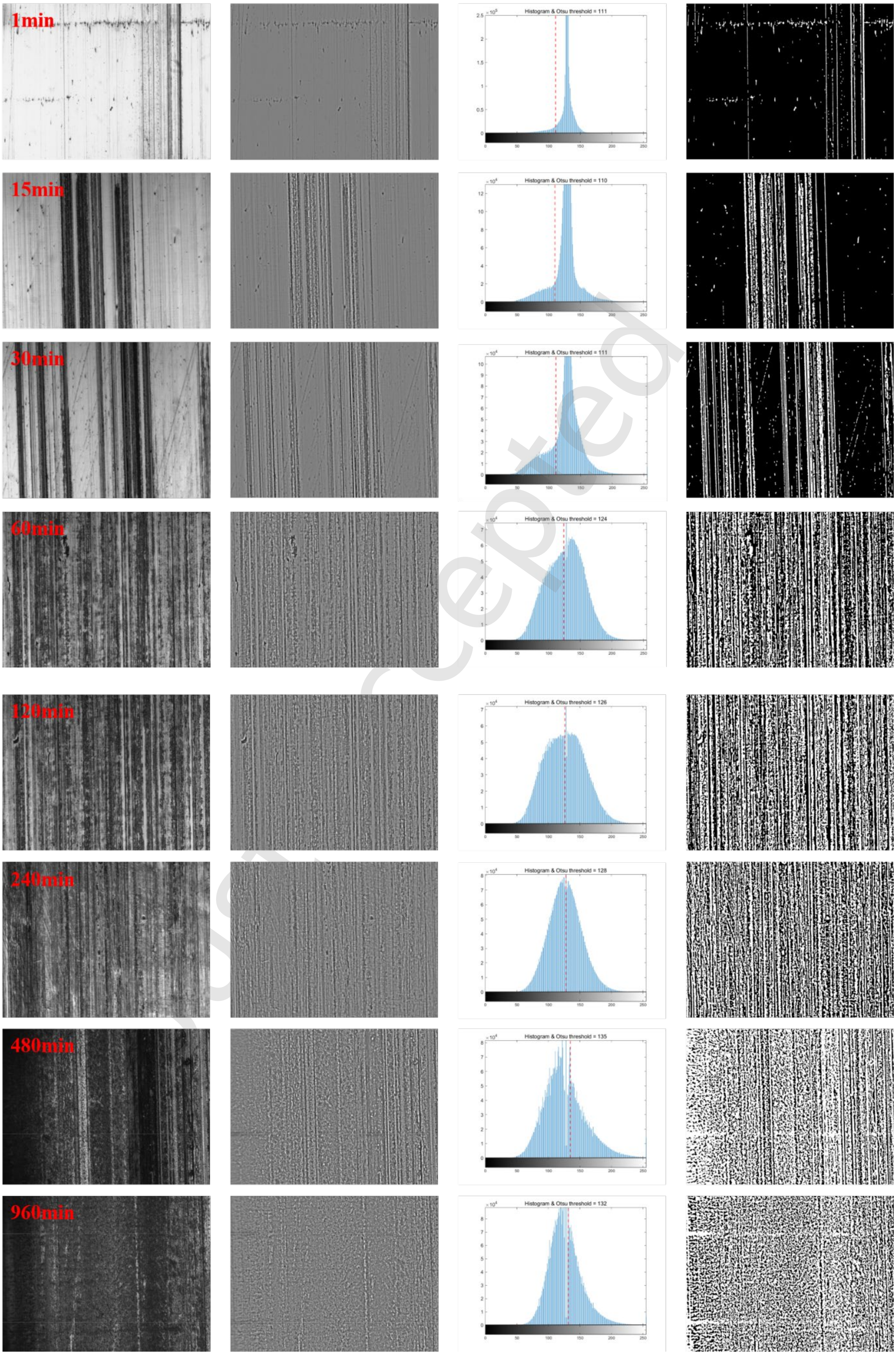
1min
Histogram & Otsu threshold = 111
15min
Histogram & Otsu threshold = 110
30min
Histogram & Otsu threshold = 111
60min
Histogram & Otsu threshold = 124
120min
Histogram & Otsu threshold = 126
240min
Histogram & Otsu threshold = 128
480min
Histogram & Otsu threshold = 135
960min
Histogram & Otsu threshold = 132

References

[1] Mohamed E S. Performance analysis and condition monitoring of ICE piston-ring based on combustion and thermal characteristics. *Applied Thermal Engineering* **132**: 824-840 (2018)

[2] Yang D, Zhang H, Wang X, Wang F , Gao G. Multi-objective prediction and optimization of working condition parameters for piston rod cap seal in Stirling engine. *Journal of Mechanical science and Technology* **38**(12): 6817-6839 (2024)

[3] Meng Y, Xu J, Jin Z, Prakash B , Hu Y. A review of recent advances in tribology. *Friction* **8**(2): 221-300 (2020)

[4] Yang M, Zhang Z, Yuan J, Wu L, Zhao X, Guo F, Men X , Liu W. Fabrication of PTFE/Nomex fabric/phenolic composites using a layer-by-layer self-assembly method for tribology field application. *Friction* **8**(45): 335-342 (2020)

[5] Kim D-J, Park Y-C, Sim K. Development and Validation of an Improved Quasisteady Flow Model with Additional Parasitic Loss Effects for Stirling Engines. *International Journal of Energy Research* **2024**(1): 8896185 (2024)

[6] Moh'd A-N, A. K S , Hashem A-O. Novel techniques to enhance the performance of Stirling engines integrated with solar systems. *Renewable Energy* **202**: 894-906 (2023)

[7] Jia X, Jung S, Haas W , Salant R F. Numerical simulation and experimental study of shaft pumping by laser structured shafts with rotary lip seals. *Tribology International* **44**(5): 651-659 (2011)

[8] Sun W, Ye J, Jiao Y , Liu X. Nanofiller tribochemical functionality is not sufficient to achieve ultralow wear of PTFE. *Wear* : 548-549 (2024)

[9] Yap K K, Fukuda K, Amspacher L, Pero R, Randall N , Masen M. Humidity-induced tribofilms of unfilled PTFE. *Wear* : 584-585 (2026)

[10] Ehsan D, Ghiyasi T N, Shahryar Z , Hanif S. An Analytical Investigation of a Thermoacoustic stirling Engine. *Arabian Journal for Science and Engineering* **49**(8): 11073-11090 (2024)

[11] Kongtragool B , Wongwises S. A review of solar-powered Stirling engines and low temperature differential Stirling engines. *Renewable and Sustainable Energy Reviews* **7**(2): 131-154 (2003)

[12] Yang X-B, Jin X-Q, Du Z-M, Cui T-S , Yang S-K. Frictional behavior investigation on three types of PTFE composites under oil-free sliding conditions. *Industrial Lubrication and Tribology* **61**(5): 254-260 (2009)

[13] Majumdar A , Bhushan B. Fractal Model of Elastic-Plastic Contact Between Rough Surfaces. *Journal of Tribology* **113**(1): 1-11 (1991)

[14] Yan W , Komvopoulos K. Contact analysis of elastic-plastic fractal surfaces. *Journal of applied physics* **84**(7): 3617-3624 (1998)

[15] Zhou G, Leu M-C , Blackmore D. Fractal geometry model for wear prediction. *Wear* **170**(1): 1-14 (1993)

[16] Ding X, Zhang Z, Ren Q, Bai C , Wang P. Abrasive Wear Prediction Model Based on Fractal Theory. *Journal of Gansu Sciences* **28**(05): 84-88 (2016)

[17] Kogut L , Etsion I. Elastic-plastic contact analysis of a sphere and a rigid flat. *Journal of applied Mechanics* **69**(5): 657-662 (2002)

[18] Morag Y , Etsion I. Resolving the contradiction of asperities plastic to elastic mode transition in current contact models of fractal rough surfaces. *Wear* **262**(5-6): 624-629 (2007)

[19] Schall J D, Gao G , Harrison J A. Effects of Adhesion and Transfer Film Formation on the Tribologv of Self-Mated DLC Contacts. *The journal of physical chemistry, C. Nanomaterials and interfaces* **114**(12): 5321-5330 (2010)

[20] K. F. Polymer composites for tribological applications. *Advanced Industrial and Engineering Polymer Research* **1**(1): 3-39 (2018)

[21] Haidar D R, Ye J, Moore A C, et al. Assessing quantitative metrics of transfer film quality as indicators of polymer wear performance. *Wear* **380**: 78-85 (2017)

[22] Ye J, Yao S, Sun W, et al. Bridging asperity adhesive wear and macroscale material transfer.

Tribology International **174**: 107768 (2022)

[23] Jiang S , Zheng Y. An analytical model of thermal contact resistance based on the Weierstrass-Mandelbrot fractal function. *Proceedings of the Institution of Mechanical Engineers, Part C: Journal of Mechanical Engineering Science* **224**(4): 959-967 (2010)

[24] Komvopoulos K , Yan W. A fractal analysis of stiction in microelectromechanical systems. *Journal of Tribology* **119**(3): 391-400 (1997)

[25] Majumdar A , Tien C. Fractal characterization and simulation of rough surfaces. *Wear* **136**(2): 313-327 (1990)

[26] Chang W, Etsion I , Bogy D B. An elastic-plastic model for the contact of rough surfaces. (1987)

[27] Wang S , Komvopoulos K. A fractal theory of the interfacial temperature distribution in the slow sliding regime: Part I-Elastic contact and heat transfer analysis. *Journal of Tribology* **116**(4): 812-822 (1994)

[28] Lin P, Xie G, Kang J, Sun X, Zhang L, He S , Cao J. Effect and performance analysis of different surface treatments on polymer-metal friction pairs. *Tribology International* **195:** 109602- (2024)

[29] Yang S, Liu Z, Zhang S, Wang W, Huang G, Lu L , Xie Y. Self-lubricating film formation and ultra-low wear of PTFE/aluminum through anodization induced nano-microtextures. *Tribology International* **208:** 110657- (2025)

[30] Li Z, Cao W, Geng J, Liu J, Wang H, Liu C, Tang H , Qi X. Synergistic effects of PEEK and PTFE on tribological properties of epoxy composites. *Tribology International* **215**(PA): 111444 (2026)

[31] Gong W, Chen Y, Li M , Kang R. Adhesion-fatigue dual mode wear model for fractal surfaces in AISI 1045 cylinder-plane contact pairs. *Wear* **430-431**(C): 327-339 (2019)

[32] Jun-Wan S, Hu-Tian F, Chang-Guang Z, Zeng-Tao C , Yi O. A new two-stage degradation model for the preload of ball screws considering geometric errors. *Wear*: 500-501 (2022)

[33] Zhimin Z, Xuexing D, Jie X, Haitao J, Ning L , Jiaxin S. A study on building and testing fractal model for predicting end face wear of Aeroengine's floating ring seal. *Wear*: 532-533 (2023)

[34] Shen J-W, Feng H-T, Zhou C-G, Chen Z-T , Ou Y. A new two-stage degradation model for the preload of ball screws considering geometric errors. *Wear*: 204352- (2022)

[35] Yuan Q, Bugong S, Honggang W, Yang Z, Gui G, Peng Z , Xiaobao Z. Quantitative Measurement of Morphological Characteristics of PTFE Composite Transfer Films Based on Computer Graphics. *Materials* **16**(4): 1688-1688 (2023)

Dongya Yang received his B.S. degree in Mechanical and Electronic Engineering from Gansu University of Technology in 2001, his M.S. degree in Mechanical Design and Theory from Donghua University in 2007, and his Ph.D. degree in Mechanical Manufacturing and Automation from Lanzhou University of Technology in 2013. He is currently an Associate Professor and Master's Supervisor at the School of Mechanical and Electrical Engineering, Lanzhou University of Technology, where he also serves as the Director of the Engineering Training Center. His research interests mainly focus on sealing technology for Stirling engines in dish-type solar thermal power systems, tribological behavior of sealing materials, and modeling and analysis of friction and wear. His work also involves mechanical system error analysis, simulation, and optimal accuracy allocation.